

# Visualizing mammalian brain area interactions by dual-axis two-photon calcium imaging

Jérôme Lecoq<sup>1</sup>, Joan Savall<sup>1,2</sup>, Dejan Vučinić<sup>1</sup>, Benjamin F Grewe<sup>1</sup>, Hyun Kim<sup>1</sup>, Jin Zhong Li<sup>1</sup>, Lacey J Kitch<sup>1</sup> & Mark J Schnitzer<sup>1-3</sup>

**Fluorescence Ca<sup>2+</sup> imaging enables large-scale recordings of neural activity, but collective dynamics across mammalian brain regions are generally inaccessible within single fields of view. Here we introduce a two-photon microscope possessing two articulated arms that can simultaneously image two brain areas (~0.38 mm<sup>2</sup> each), either nearby or distal, using microendoscopes. Concurrent Ca<sup>2+</sup> imaging of ~100–300 neurons in primary visual cortex (V1) and lateromedial (LM) visual area in behaving mice revealed that the variability in LM neurons' visual responses was strongly dependent on that in V1, suggesting that fluctuations in sensory responses propagate through extended cortical networks.**

Two-photon Ca<sup>2+</sup> imaging has become a vital tool for monitoring the dynamics of large numbers of neurons in behaving animals<sup>1,2</sup>. However, a conventional two-photon microscope is usually limited to fields of view <600 μm wide and confined to a single area of the mammalian brain. This approach has been fruitful for studies of local microcircuitry, but neuroscientists have been hard pressed to image interactions across pairs of brain areas in a way that simultaneously provides cellular resolution within each area. Recent work has shown the feasibility of *in vivo* Ca<sup>2+</sup> imaging within presynaptic axonal inputs originating from anatomically defined areas<sup>3</sup>, but it has not been feasible, to date, to combine this with Ca<sup>2+</sup> imaging of the postsynaptic responses. Overall, there has been an unmet need for imaging technology that can monitor the dynamics of many individual cells of two or more brain areas in behaving animals. Such technology will be crucial for studying how inter-area network interactions shape behavior and cognition and understanding how cells in distinct regions coordinate their dynamics.

## RESULTS

Here we initiate imaging studies of multi-area interactions at cellular resolution by introducing a two-photon microscope with two movable imaging arms. This dual-axis microscope can image neural activity simultaneously in two nearby or distal brain areas in a head-restrained behaving mouse (**Fig. 1** and **Supplementary Fig. 1a–d**). Although it is likely that many researchers have considered such an approach, a longstanding technical barrier has concerned how to bring the optical

foci of two imaging arms into close proximity so that even two nearby brain areas can be imaged without physical collisions between the two objective lenses. As illustration of the issue's importance, anatomical regions in mouse neocortex corresponding to successive stages of cortical processing are typically separated by distances of ~1 mm or less. For two specimen planes of such minimal separation, it is generally not possible to position two conventional, high-resolution microscope objective lenses in a suitable mechanical arrangement around the cranium of a behaving mouse.

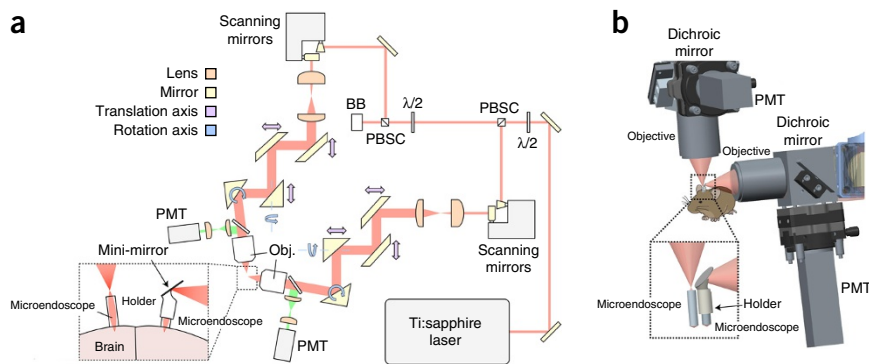
The crucial insight underlying the dual-axis microscope was that objective lenses equipped with ancillary micro-optics could permit sufficiently close positioning of the two optical arms to permit concurrent imaging of brain areas separated by as little as ~1 mm. Miniaturized epifluorescence microscopes based on micro-optics have recently allowed Ca<sup>2+</sup> imaging in freely behaving mice<sup>4,5</sup>, so we were familiar with the capabilities of microlenses to capture fluorescence signals, often at sufficient resolution to resolve individual dendrites. Here we reasoned that these advances in micro-optic imaging should enable a dual-axis two-photon microscope with a pair of micro-optical objective lenses that can be placed in close proximity on the head of a live mouse, without physical collision.

To accomplish this, we developed microendoscopes with an optical design that was distinct from those used previously<sup>4-7</sup> and expressly intended for holistic optimization of a dual-axis instrument for *in vivo* Ca<sup>2+</sup> imaging. Each microscope arm had a custom-designed, doublet gradient refractive index (GRIN) microendoscope. Each doublet had a 0.5 numerical aperture (NA) GRIN micro-objective to provide adequate resolution and collection of fluorescence emissions. A customized, 0.35 NA GRIN relay microlens enabled high-efficiency optical coupling to a conventional, long-working distance microscope objective lens (24 mm working distance (WD), 0.35 NA, Nikon) positioned >2 cm away from the mouse's head. The higher NA of this GRIN relay compared to typical values (0.1–0.2) allowed us to choose a long-working-distance microscope objective of sufficient NA (0.35) to maintain satisfactory resolution (limited by the 0.5 NA of the GRIN objective) over a broad field of view (approximately proportional to the ratio 0.35:0.5). To allow collision-free movement of the two independent microscope arms and their objective lenses, on one of the microendoscopes we placed a miniature circular mirror (3 mm diameter)

<sup>1</sup>James H. Clark Center for Biomedical Engineering & Sciences, Stanford University, Stanford, California, USA. <sup>2</sup>Howard Hughes Medical Institute, Stanford University, Stanford, California, USA. <sup>3</sup>CNC Program, Stanford University, Stanford, California, USA. Correspondence should be addressed to M.J.S. ([mschnitz@stanford.edu](mailto:mschnitz@stanford.edu)) or J.L. ([jlecoq@stanford.edu](mailto:jlecoq@stanford.edu)).

Received 4 August; accepted 10 October; published online 17 November 2014; doi:10.1038/nn.3867

**Figure 1** A two-photon microscope with microendoscopes and two optical axes for imaging two brain areas in awake behaving mice. **(a)** Schematic of the optical pathway. The beam from an infrared ultrashort-pulsed Ti:sapphire laser is divided into two beams using polarizing beam splitters (PBSC). Rotatable half-wave ( $\lambda/2$ ) plates control the power of each beam independently; a beam block (BB) absorbs the unused power. Two pairs of scanning mirrors independently sweep each beam across the two individual specimen planes. Each arm of the microscope has three remotely controlled motorized stages providing three translational degrees of mechanical freedom. Each arm also has two rotational degrees of freedom that are adjusted manually. To allow the two chosen brain areas under view to be either distal or nearby, two microscope objective lenses focus the two beams into a pair of microendoscopes (0.5 NA), which in turn focus the laser beam onto tissue. Visible fluorescence emissions return through the microendoscopes and objective lenses and reflect off dichroic mirrors. Photomultiplier tubes (PMT) detect the fluorescence signals. Inset, the two microendoscopes focus the two beams onto the chosen brain areas and collect fluorescence signals. One microendoscope has a holder that bears a miniature mirror folding its incoming beam by 90°; this arrangement allows the objectives to be placed close to each other without collision. **(b)** Schematic of the mechanical design. Inset, magnified view of the mechanisms for delivery of the laser beams to the brain areas. The mouse is roughly to scale. Obj., objective.



on the GRIN relay lens, folding the optical pathway by 90° (**Fig. 1** and **Supplementary Fig. 1d**). This right-angle fold in one arm allowed its microscope objective lens to approach the mouse from a sideways vantage, freeing the space around the mouse head for ancillary apparatus such as for head restraint and sensory stimulation (**Fig. 1b**). The use of long-working-distance air objectives further helped to provide ample room (Online Methods).

Apart from the two orthogonally oriented objective lenses, the rest of the instrument resembled a pair of two-photon microscopes that share a single titanium-sapphire (Ti:sapphire) laser but have their own photomultiplier tubes and laser-scanning mirrors (**Fig. 1a** and **Supplementary Fig. 1**). The maximum power of ~142 mW at each specimen plane implied an overall efficiency of 23% in illumination delivery, given our laser’s power of 1.24 W when tuned for 915 nm emission. We characterized each arm’s optical point-spread function by imaging 170-nm-diameter fluorescent beads, and thereby determined the optical resolution (FWHM) limits for 910 nm illumination (lateral:  $1.03 \pm 0.02 \mu\text{m}$  and  $0.97 \pm 0.02 \mu\text{m}$ ; axial:  $9.8 \pm 0.2 \mu\text{m}$  and  $7.9 \pm 0.3 \mu\text{m}$ ; mean  $\pm$  s.e.m.;  $n = 7$  beads, for the arms without and with the miniature mirror, respectively). These resolution values for 910 nm light are comparable to those measured previously for GRIN microendoscopes using 790–810 nm light<sup>8,9</sup> and thereby highlight the merits of the present customized probes.

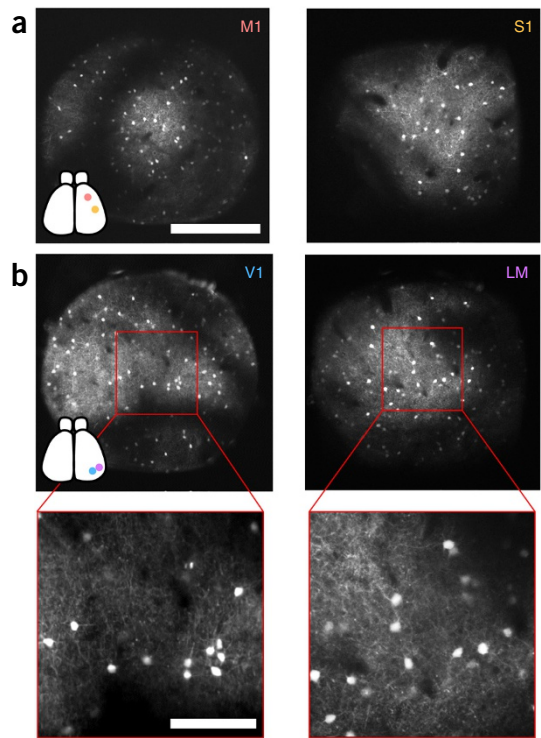
Together, the two arms had sufficient mechanical freedom to image nearly any two brain areas in the mouse that can be accessed individually with a GRIN microendoscope. Each arm had two degrees of rotational and three degrees of translational movement (**Fig. 1a** and **Supplementary Fig. 1c**). Using computer simulations (Online Methods and **Supplementary Fig. 1b,c**), we minimized mechanical collisions that might result during the broad set of possible movements within the ten mechanical degrees of freedom. These simulations of the mechanics revealed that all ten degrees of freedom were essential to permit the optical alignment of each arm to its GRIN microendoscope (Online Methods). With any fewer degrees of freedom, the simulations showed one loses the ability to choose any two brain areas for imaging, confirming that a pair of conventional microscopes with less than ten total degrees of freedom would be inadequate. Some commercial microscopes provide modest mechanical flexibility, but with insufficient freedom to allow the simultaneous optical alignment of both microendoscopes. Further, without specifically optimizing the collective design,

the use of two arms that were intended merely for individual use will lead to mechanical collisions for many pairs of brain areas. Finally, commercial two-photon microscopes typically optimize resolution at the expense of power efficiency, whereas our goal was to attain cellular resolution across two fields-of-view using a single Ti:sapphire laser.

As an initial test, we first sought to image two brain areas in anesthetized mice expressing the red fluorophore TdTomato<sup>10</sup> in parvalbumin interneurons. To illustrate flexibility of usage, we examined a pair of neocortical areas (motor area M1 and somatosensory area S1) separated by ~3.5 mm (**Fig. 2a**), and another pair (visual areas V1 and LM) that were adjacent and separated by only ~1.2 mm (**Fig. 2b**). On the day of imaging we brought the two GRIN microendoscopes to the two neocortical areas of the anesthetized mouse. After optical alignment of each imaging arm to its microendoscope, we visualized layer 2/3 parvalbumin neurons in the two brain areas simultaneously. All images revealed individual cell bodies and dendrites (**Fig. 2**). Notably, all ten mechanical degrees of freedom were essential to permit imaging in S1 and M1, or in V1 and LM (which is probably homologous to V2 in primates)<sup>11</sup>, in the same cerebral hemisphere. Moreover, microendoscopy is already well established as a means of imaging deep brain areas<sup>5–7</sup>. To illustrate that our dual-axis approach also enables studies in which one or both of the brain areas lie below the neocortex, we imaged TdTomato-expressing parvalbumin interneurons simultaneously in the frontal cortex and CA1 area of hippocampus (**Supplementary Fig. 2**).

To demonstrate simultaneous Ca<sup>2+</sup> imaging in two functionally related brain areas, we focused on the visual cortex. The mouse visual cortex contains at least ten distinct areas, each with its own retinotopic map<sup>12,13</sup>. To understand how these areas coordinate visual information processing, it is important to observe them at work simultaneously in the behaving animal. To do this, we first injected into the right visual cortex an adeno-associated viral vector to express the genetically encoded Ca<sup>2+</sup> indicator GCaMP6s in pyramidal neurons under the control of the *Camk2a* promoter<sup>14</sup>. One month later we mapped the retinotopy of three to four visual areas surrounding and including V1 by low-magnification two-photon Ca<sup>2+</sup> imaging in head-restrained mice at liberty to run on a trackball (Online Methods). To aid the interpretation of cellular imaging data, we also performed control experiments to verify that the axial resolution values of our dual-axis microscope sufficed to prevent crosstalk from out-of-focal

**Figure 2** The dual-axis microscope permits imaging of either distal or nearby brain regions. **(a)** Simultaneously acquired images of two distal neocortical areas (M1 and S1; ~3.5 mm apart) in an anesthetized mouse expressing tdTomato in parvalbumin interneurons. Inset, schematic of the relative locations of M1 (pink dot) and S1 (yellow dot) in the right cerebral hemisphere. **(b)** Simultaneously acquired images of two proximal visual cortical areas (V1 and LM; ~1.2 mm separation). The microscope can image broad fields of view (top, 708  $\mu$ m across) and can also zoom in on neuronal processes (bottom, 264  $\mu$ m across). Inset, schematic of the locations of V1 (blue dot) and LM (purple dot). Scale bars, 300  $\mu$ m (**a** and **b**, top) and 100  $\mu$ m (**b**, bottom).



plane neuronal cell bodies, dendrites or axons (**Supplementary Figs. 3 and 4** and **Online Methods**). We then used the dual-axis microscope to concurrently monitor layer 2/3 neuronal  $Ca^{2+}$  dynamics in areas V1 and LM while a video monitor displayed moving gratings in front of the mouse's left eye (**Supplementary Video 1**).

In this configuration, we simultaneously monitored ~100–300 layer 2/3 neurons in each visual area (**Fig. 3a–c**). After we zoomed in with the laser-scanning pattern to obtain higher-magnification images, we found that dendrites and their  $Ca^{2+}$  dynamics were readily visible (**Supplementary Fig. 5** and **Supplementary Video 1**). While the mouse rested or moved voluntarily on the track ball, a video monitor (centered over the left eye) presented moving gratings (0.035 cycles per degree of visual space, progressing at 1.25 Hz). The gratings moved in one of four orthogonal directions, randomly chosen with equal probability for each 6-s trial. Dual-area imaging sessions lasted ~30 min, permitting us to record from V1 and LM across 200 trials of moving grating presentation.

We extracted the spatial locations and fluorescence time traces of neurons displaying  $Ca^{2+}$  transients in the movie data using an

established cell-sorting algorithm based on principal and independent component analyses<sup>4,5,15</sup> (**Online Methods**). Each brain area yielded ~100–300 neuronal cell bodies exhibiting  $Ca^{2+}$  activity (90–301 cells in V1, mean 162; 70–180 cells in LM, mean 103;  $n = 7$  mice). Mean rates

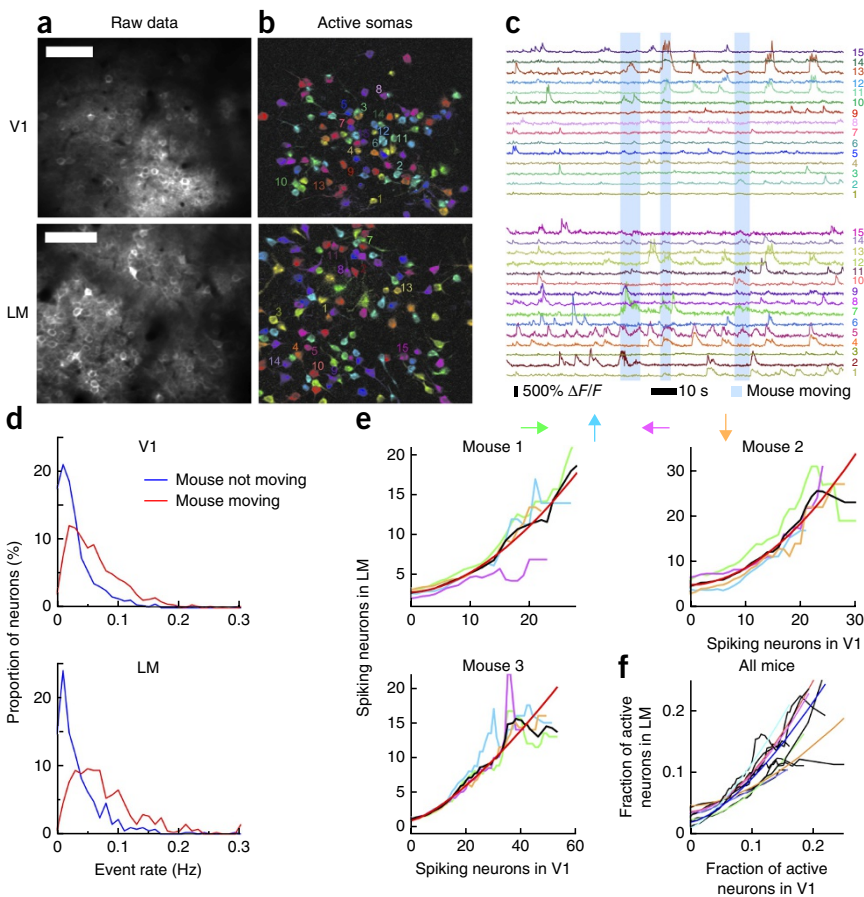


**Figure 3**  $Ca^{2+}$  imaging in awake behaving mice reveals that neurons in visual areas V1 and LM exhibit supralinear inter-area correlations. **(a)** Simultaneous  $Ca^{2+}$  imaging of V1 and LM in head-restrained mice at liberty to walk or run on a trackball. Grayscale images are time averages over 5 min of movie data. **(b,c)** Color images of neuronal cell bodies that showed  $Ca^{2+}$  activity **(b)** and corresponding time traces of  $Ca^{2+}$  dynamics for 15 V1 and 15 LM cells **(c)**. Blue shaded epochs **(c)** denote periods of mouse locomotion. **(d)** Histograms of the mean rates of  $Ca^{2+}$  transients (cell bodies and processes combined) from four mice (864 V1 neurons and 418 LM neurons in total) during periods of mouse locomotor activity and rest. **(e)** The number of neurons active in LM within 1-s time windows is a supralinear function of the number of pyramidal cells concurrently active in V1, under identical conditions of visual presentation, for each of the four directions of grating movement. Traces' colors correspond to those of the arrows, which indicate the direction of grating motion. Black traces show averages over all directions of grating movement for each mouse. Red traces show three-parameter fits to the form  $f(x) = a + bx^c$ . **(f)** The supralinear dependence shown in **e** is present in all seven mice examined. Each black trace is the average over all grating directions for one mouse. The colored traces show the corresponding parametric fits, with each color denoting an individual mouse. Scale bars, 100  $\mu$ m (bars apply to **a** and **b**).



of somatic  $\text{Ca}^{2+}$  activity in V1 and LM during visual stimuli depended significantly on the mouse's behavioral state, rising respectively from  $0.032 \pm 0.001 \text{ s}^{-1}$  (mean  $\pm$  s.e.m.) and  $0.035 \pm 0.002 \text{ s}^{-1}$  when the mouse was resting, to  $0.06 \pm 0.002 \text{ s}^{-1}$  and  $0.08 \pm 0.003 \text{ s}^{-1}$  during locomotor behavior (two-tailed sign test;  $P < 10^{-39}$  for both V1 ( $n = 684$  cells) and LM ( $n = 344$  cells);  $n = 4$  mice) (Fig. 3d). This finding is consistent with prior studies reporting a rise in the mean activity of mouse area V1 neurons during locomotor behavior<sup>12,16,17</sup> and reveals that a similar effect occurs in area LM.

In addition to neuronal somata, the cell-sorting algorithm also yielded up to  $\sim 100$  other independent components representing neuronal processes that showed  $\text{Ca}^{2+}$  activation (0–112 processes in V1, mean 41; 0–43 processes in LM, mean 21;  $n = 7$  mice). Rates of  $\text{Ca}^{2+}$  activation in neuronal processes also rose significantly during locomotion, from  $0.026 \pm 0.002 \text{ s}^{-1}$  and  $0.030 \pm 0.004 \text{ s}^{-1}$  in V1 and LM (mean  $\pm$  s.e.m.), respectively, to  $0.062 \pm 0.003 \text{ s}^{-1}$  and  $0.068 \pm 0.004 \text{ s}^{-1}$  (two-tailed sign test;  $P < 10^{-11}$  for both V1 ( $n = 180$  processes) and LM ( $n = 74$  processes);  $n = 4$  mice). Active cell bodies and processes generally both showed visual orientation tuning and had  $\text{Ca}^{2+}$  responses of substantially different magnitudes for gratings moving in different directions (Supplementary Fig. 6). Overall, using the dual-axis microscope we confirmed results from prior studies that examined V1 and LM individually in behaving mice. This provided the necessary validation to analyze inter-area effects that would be apparent only in simultaneous multi-neuronal recordings from the two brain areas.

As a first analysis of how V1 and LM interact, we examined the variability in the number of neurons that were simultaneously active in each brain area under uniform conditions of visual stimulation (Fig. 3e,f). For each direction of grating motion, the number of active LM neurons (1 s time bins) was a nonlinear function of the number of active V1 neurons that was well fit by a three-parameter, fractional polynomial function of the form  $f(x) = a + bx^c$ . The value of the exponent  $c$  ranged from 1.3–1.9, but was approximately the same in each individual mouse for all four directions of grating movement (mean value,  $1.6 \pm 0.1$  s.e.m.,  $n = 7$  mice; mean reduced chi-squared = 1.1) (Fig. 3e). In all seven mice analyzed in detail, under uniform conditions of stimulus presentation on the video monitor we found a supralinear relationship between the level of activity in V1 and that in LM (Fig. 3f). For comparison, we tested whether a three-parameter, threshold-linear function ( $f(x) = a$  for  $x < x_0$ ;  $f(x) = a + b(x - x_0)$  for  $x \geq x_0$ ) could also account for this observed nonlinearity. However, the mean reduced chi-squared value was substantially higher (2.0) than for the fractional polynomial model, and in five of seven mice the fit with the fractional polynomial was superior to an extent that was statistically significant ( $F$ -test;  $P < 0.1$ ). The favorable reduced chi-squared values obtained with the fractional polynomial show that this model successfully captures the measured inter-relationship between V1 and LM; however there are probably other (untested) parametric models that would perform similarly well.

## DISCUSSION

We used a pair of customized microendoscopes to monitor two neocortical regions concurrently, illustrated by imaging M1 and S1, as well as by functional imaging in V1 and LM, in mice free to run on a trackball. The key engineering insight was that a pair of microendoscopes can address two brain areas, distal or nearby, without mechanical collisions between the two imaging arms. This innovation builds on the established utility of microendoscopes as a means of imaging deep brain areas<sup>6,7</sup>, and our dual-axis approach is compatible with studies in which one or both of the brain areas lie below the neocortex. Thus, given its capabilities for imaging distal pairs and deep brain

areas, our instrument provides a general solution to the challenge of imaging two brain regions concurrently.

Our joint  $\text{Ca}^{2+}$  imaging studies in visual cortical areas V1 and LM of behaving mice revealed that, under uniform conditions of visual stimulation, the number of active neurons in LM has a supralinear dependence on the number of active neurons in V1. Given that V1 is upstream of LM in the visual cortex, this result suggests that momentary fluctuations in visually evoked neural responses in V1 can propagate to area LM. There are many possible causes of such fluctuations in V1, including stochastic aspects of single cell dynamics, fluctuations in network state, variations in the mouse's behavior or gaze direction and combinations thereof. Regardless of how such fluctuations arise in V1, one attractive explanation for the supralinearity of the relationship with LM stems from a straightforward combination of single neurons' properties in LM and their retinotopic inputs from V1. Prior experimental and theoretical work suggests that neocortical pyramidal cells' dendrites perform a supralinear summation of their synaptic inputs<sup>18,19</sup>. In the present experiment, the LM neurons under view are likely to share many common inputs from V1. Thus, as activity rates rise in V1 neurons providing inputs to LM, supralinear summation of these inputs within LM cells' dendrites should yield a supralinear dependence of LM cells' firing rates on those in V1. Although our data are consistent with this simple explanation, more experiments are needed to explore these issues in depth. Nevertheless, the supralinear relationship we observed between LM and V1 offers a mathematical constraint on models of visual cortical computation. This observation regarding the simultaneous network level dynamics in two areas of the visual system is but an initial example of how dual-axis microscopy will help neuroscientists probe local and global information processing in behaving animals.

We expect that, with additional engineering, brain imaging using three or more articulated optical arms will be feasible in behaving animals. Although it is probably prohibitive to have three or more conventional objective lenses focused on the mouse's head, the use of miniature objective lenses or even entire laser-scanning systems that have been miniaturized has grown more commonplace in neuroscience research<sup>9,20–22</sup>. Such miniaturized elements work well for *in vivo*  $\text{Ca}^{2+}$  imaging<sup>21,22</sup> and will be far easier to distribute around the cranium than conventional objective lenses. Given the recent expansion in behavioral assays for head-restrained rodents<sup>1,2,23</sup>, our work points the way to a wide set of future studies probing brain area interactions in sensory, cognitive and motor tasks, and the computational transformations enacted across brain areas.

## METHODS

Methods and any associated references are available in the [online version of the paper](#).

Note: Any Supplementary Information and Source Data files are available in the [online version of the paper](#).

## ACKNOWLEDGMENTS

We thank K. Merkle for machining the various custom parts of the microscope, S. Sinha for help with coating miniature mirrors, and J. Li for help with histology and mouse husbandry and genotyping. We appreciate support from a Stanford Vision Translation Postdoctoral Fellowship (J.L.), a Swiss National Postdoctoral Fellowship (B.F.G.), graduate research fellowships from the US National Science Foundation, Stanford University and the Simons Foundation (L.J.K.) and research funding from a US National Institutes of Health (NIH) EUREKA grant (M.J.S.) and the NIH NDC for the Optical Control of Biological Function (J.L. and M.J.S.).

## AUTHOR CONTRIBUTIONS

J.L., D.V. and M.J.S. initiated the project. J.L., J.S., D.V. and M.J.S. designed the microscope. J.L., B.F.G. and H.K. performed experiments. J.Z.L. prepared

and titrated viral vectors. J.L. and L.J.K. performed analysis. J.L. and M.J.S. wrote the manuscript. All authors reviewed the manuscript. M.J.S. supervised the project.

#### COMPETING FINANCIAL INTERESTS

The authors declare no competing financial interests.

Reprints and permissions information is available online at <http://www.nature.com/reprints/index.html>.

- Dombeck, D.A., Khabbaz, A.N., Collman, F., Adelman, T.L. & Tank, D.W. Imaging large-scale neural activity with cellular resolution in awake, mobile mice. *Neuron* **56**, 43–57 (2007).
- Nimmerjahn, A., Mukamel, E.A. & Schnitzer, M.J. Motor behavior activates Bergmann glial networks. *Neuron* **62**, 400–412 (2009).
- Glickfeld, L.L., Andermann, M.L., Bonin, V. & Reid, R.C. Cortico-cortical projections in mouse visual cortex are functionally target specific. *Nat. Neurosci.* **16**, 219–226 (2013).
- Ghosh, K.K. *et al.* Miniaturized integration of a fluorescence microscope. *Nat. Methods* **8**, 871–878 (2011).
- Ziv, Y. *et al.* Long-term dynamics of CA1 hippocampal place codes. *Nat. Neurosci.* **16**, 264–266 (2013).
- Barretto, R.P. *et al.* Time-lapse imaging of disease progression in deep brain areas using fluorescence microendoscopy. *Nat. Med.* **17**, 223–228 (2011).
- Jung, J.C., Mehta, A.D., Aksay, E., Stepnoski, R. & Schnitzer, M.J. *In vivo* mammalian brain imaging using one- and two-photon fluorescence microendoscopy. *J. Neurophysiol.* **92**, 3121–3133 (2004).
- Jung, J.C. & Schnitzer, M.J. Multiphoton endoscopy. *Opt. Lett.* **28**, 902–904 (2003).
- Flusberg, B.A., Jung, J.C., Cocker, E.D., Anderson, E.P. & Schnitzer, M.J. *In vivo* brain imaging using a portabler3. r3.9 gram two-photon fluorescence microendoscope. *Opt. Lett.* **30**, 2272–2274 (2005).
- Shaner, N.C. *et al.* Improved monomeric red, orange and yellow fluorescent proteins derived from *Discosoma* sp. red fluorescent protein. *Nat. Biotechnol.* **22**, 1567–1572 (2004).
- Wang, Q., Sporns, O. & Burkhalter, A. Network analysis of corticocortical connections reveals ventral and dorsal processing streams in mouse visual cortex. *J. Neurosci.* **32**, 4386–4399 (2012).
- Andermann, M.L., Kerlin, A.M., Roumis, D.K., Glickfeld, L.L. & Reid, R.C. Functional specialization of mouse higher visual cortical areas. *Neuron* **72**, 1025–1039 (2011).
- Marshel, J.H., Garrett, M.E., Nauhaus, I. & Callaway, E.M. Functional specialization of seven mouse visual cortical areas. *Neuron* **72**, 1040–1054 (2011).
- Chen, T.W. *et al.* Ultrasensitive fluorescent proteins for imaging neuronal activity. *Nature* **499**, 295–300 (2013).
- Mukamel, E.A., Nimmerjahn, A. & Schnitzer, M.J. Automated analysis of cellular signals from large-scale calcium imaging data. *Neuron* **63**, 747–760 (2009).
- Niell, C.M. & Stryker, M.P. Modulation of visual responses by behavioral state in mouse visual cortex. *Neuron* **65**, 472–479 (2010).
- Keller, G.B., Bonhoeffer, T. & Hubener, M. Sensorimotor mismatch signals in primary visual cortex of the behaving mouse. *Neuron* **74**, 809–815 (2012).
- Waters, J., Larkum, M., Sakmann, B. & Helmchen, F. Supralinear Ca<sup>2+</sup> influx into dendritic tufts of layer 2/3 neocortical pyramidal neurons *in vitro* and *in vivo*. *J. Neurosci.* **23**, 8558–8567 (2003).
- Polsky, A., Mel, B.W. & Schiller, J. Computational subunits in thin dendrites of pyramidal cells. *Nat. Neurosci.* **7**, 621–627 (2004).
- Piyawattanametha, W. *et al.* *In vivo* brain imaging using a portabler2. r2.9-g two-photon microscope based on a microelectromechanical systems scanning mirror. *Opt. Lett.* **34**, 2309–2311 (2009).
- Helmchen, F., Denk, W. & Kerr, J.N. Miniaturization of two-photon microscopy for imaging in freely moving animals. *Cold Spring Harb. Prot.* **2013**, 904–913 (2013).
- Sawinski, J. *et al.* Visually evoked activity in cortical cells imaged in freely moving animals. *Proc. Natl. Acad. Sci. USA* **106**, 19557–19562 (2009).
- Dombeck, D.A., Harvey, C.D., Tian, L., Looger, L.L. & Tank, D.W. Functional imaging of hippocampal place cells at cellular resolution during virtual navigation. *Nat. Neurosci.* **13**, 1433–1440 (2010).

## ONLINE METHODS

**Mice.** We used female PV-TdTomato mice and male C57BL/6 mice (aged 8–12 weeks at start; housed in reversed light-dark cycle environment; ~4 and 1 per cage before and after surgery, respectively). We generated PV-TdTomato mice by crossing a reporter line (B6;129S6-Gt(ROSA)26Sortm9(CAG-tdTomato)Hze/J, stock 007905 from Jackson labs<sup>24</sup>) with a PV-Cre driver mouse line (B6;129P2-Pvalbtm1(cre)Arbr/J, stock 008069 from Jackson labs<sup>25</sup>).

**Surgery and viral injections.** Stanford APLAC approved all procedures. We performed all surgeries under 1.5–2% isoflurane. For studies in PV-TdTomato mice we located cortical areas using stereotaxic coordinates (M1: 1.8 mm anterior and 1.8 mm lateral to bregma; S1: -1.5 mm anterior and 3.2 mm lateral; frontal association cortex (FrA): 2.6 mm anterior and 0.5 mm lateral). At each cortical imaging site we implanted a 1.27-mm-outer-diameter stainless steel cannula (89935K228, McMaster) glued to #0 coverslips cut to the same ~1.3-mm diameter. By using 2% agar and dental acrylic, we held the cannulas permanently in place on the cranium. We imaged hippocampal area CA1 (2.1 mm posterior to bregma, 2.1 mm lateral, 1.1 mm ventral) according to published microendoscopy protocols<sup>5,6</sup>.

For Ca<sup>2+</sup> imaging experiments, we used AAV2/5-CaMKII $\alpha$ -GCaMP6s to express the Ca<sup>2+</sup> indicator in pyramidal cells<sup>14</sup> (Fig. 3). To locate visual cortical areas V1 and LM, on the basis of a recent study of visual cortical maps in mice<sup>11</sup>, we used a coordinate system whose origin was the intersection between the midline and a perpendicular line drawn from the anterior border of the transverse sinus at the pole of the occipital cortex (V1: 1.1 mm anterior, 2.8 mm lateral; LM: 1.4 mm anterior, 4.1 mm lateral). We injected 500 nL of AAV2/5-CaMKII $\alpha$ -GCaMP6s ( $1.8 \times 10^{13}$  GC/ml) in C57BL/6 mice at the two chosen locations using a glass pipette with a ~20–30  $\mu$ m wide tip. After waiting at least 3 weeks, we implanted a 5-mm-diameter #0 coverslip glued to a stainless steel tube (50415K164, McMaster) over neocortex, following previously described protocols<sup>12</sup> for implantation and postsurgical care.

**Microscope design.** We created the two-armed microscope using Zemax ray tracing software for optical design. The illumination source was an ultrashort-pulsed Ti:Sapphire laser (Mai Tai BB, Spectra-Physics). We divided the primary beam in two and controlled the power of the two daughter beams using polarized beam splitter cubes (PBS052, Thorlabs) and half-wave plates (AHWP05M-980, Thorlabs) (Fig. 1). Rotary stages (PRM1Z8, Thorlabs) permitted computer control of the wave plates' angular positions and thus the power in each of the two beams.

Broadband dielectric mirrors (BB1-E03, Thorlabs) routed each beam to an independent pair of galvanometer-driven laser-scanning mirrors (6215H, Cambridge Technology). Both sets of scanning mirrors received the same command signals, which we generated in Matlab (Mathworks) using Scanimage<sup>26</sup> and a PCI bus computer card (PCI 6115, National Instruments). Lens pairs forming optical telescopes, each pair comprising an achromatic scan lens ( $f = 100$  mm, AC508-100-B-ML Thorlabs) and the other an achromatic tube lenses ( $f = 300$  mm, AC508-300-B-ML Thorlabs), imaged the two beams onto the back-apertures of a corresponding pair of microscope objective lenses (CFI L Plan Epi SLWD, 0.35 NA 20 $\times$  Nikon).

The long working distance (24 mm) of the two objective lenses afforded sufficient space to position them both near the mouse head. The objectives coupled the illumination beams into custom, 1-mm-diameter compound doublet GRIN lenses (0.31 pitch GRIN micro-objective, collection NA 0.5; relay GRIN lens 0.06 pitch, relay NA 0.2; Grintech GmbH), which we designed to provide adequate fluorescence collection (0.5 NA) over 700- $\mu$ m-wide fields of view (Supplementary Fig. 1d). To set one of the optical axes approximately parallel to the surface of the mouse cranium, we used metal vapor deposition to coat a 3-mm-diameter #0 coverslip with a reflective coating, and then we attached the resulting tiny mirror to the relay lens of one of the two GRIN microendoscopes by using UV-cured glue (NOA 81, Norland) and a custom 3D-printed holder (Fig. 1b). We positioned both microendoscopes on the mouse just before the imaging session.

A custom magnetic holder held a dichroic mirror (735 nm long-pass; FF735-Di01-29.9x39.5 Semrock) near the back aperture of each microscope objective lens. To permit fluorescence collection across the scanning mirrors' full angular ranges, a pair of aspheric lenses (NT49-103 and NT49-101, Edmund Optics)

imaged the back aperture of each objective onto the 5-mm-wide active area of a GaAsP photomultiplier tube (PMT) (H10770PA-40, Hamamatsu). To protect the PMTs from the infrared laser illumination and the blue visual stimulation to the mouse, we concatenated a 720-nm short-pass (FF01-720/SP-25-D Semrock) and a 525-nm band-pass (FF03-525/50-25 Semrock) filter in front of each PMT. We removed the band-pass filters when imaging red fluorescence emissions from TdTomato<sup>10</sup>.

We created the microscope's mechanical design using Pro/Engineer computer-assisted design software (Supplementary Fig. 1). Most components were off the shelf. Each arm of the microscope had independent mechanical capabilities with three degrees of translation (implemented by motorized stages of 50 mm range, MTS50-Z8, Thorlabs) and two degrees of rotation (implemented by manual rotary stages of 360° range, CRMIL, Thorlabs). In total, these ten degrees of freedom permitted imaging in virtually all-possible pairs of locations on the mouse head. We routed the laser beam through the articulated mechanical arms by using dielectric mirrors to maintain optical alignment in all mechanical configurations.

To attain optimal resolution and fluorescence collection efficiency, it is important to precisely align the microscope objective lens of each arm to its corresponding microendoscope. To simplify the alignment of both arms, we co-aligned the red beam of a laser diode (CPS180, Thorlabs) to the infrared beam of the Ti:sapphire laser. The red beam provided immediate visual feedback regarding the alignment status without use of an infrared viewer, which greatly eased the alignment procedure. To start, we temporarily removed each microscope objective lens, located the red beam's back-reflection off each microendoscope, and adjusted each arm's two rotational degrees of freedom so that the incoming beam was parallel to the microendoscope's optical axis. We further checked that each back-propagating red laser beam struck the center of the arm's tube lens. We then replaced the microscope objective lenses and used each arm's three translational degrees of freedom to focus the laser illumination onto the back face of each microendoscope. We found the correct alignment by turning on laser scanning at a slow speed (1–2 Hz) and ensuring that the scanning pattern of red light was centered on the back face of each microendoscope. This entire procedure took 5–20 min, depending on how far the arms' positions had changed from their previous locations.

**In vivo imaging.** We imaged the mice beginning at least 4 weeks after viral injection and 1 week after the initial surgery, and were generally able to acquire images for several months. To hold both microendoscopes on top of the cortical implant during imaging, we machined a plastic disc (4.5 mm diameter, 2 mm thick) to fit inside the 5-mm-diameter cannula. The disk had a pair of 1.2-mm-diameter holes whose locations matched the chosen brain areas, when the disk was suitably positioned within the cannula on the day of imaging. We fixed the plastic disc in place using a drop of UV-curing glue (Norland NOA 81).

We held awake mice on top of a 11.4-mm-diameter Styrofoam ball (Plasteel Corp.) using a two-point head holder, as previously described<sup>27</sup>. The ball was floating on a thin layer of water held in a plastic bowl of nearly identical diameter (Crittter-Cages). At the beginning of each imaging session, we positioned each microendoscope on the neocortex. A small drop of glycerol on the glass reduced transitions in optical index between the microendoscope and the coverslip, as compared to an air gap. After transferring the mice to the microscope, we positioned a video monitor (43.2 mm diagonal, Dell 1703FP) 100 mm from the left eye. The screen covered approximately  $\pm 60^\circ$  of field of view in both azimuth and elevation around the center of the left eye's gaze. Three layers of blue filter (Roscolux #382, Rosco) placed on top of the monitor virtually eliminated stray light of other wavelengths within the pass band of the optical filters covering the PMTs. During *in vivo* imaging, light leakage from the video monitor accounted for ~0.2% of the photocurrent from the PMTs. We monitored mouse behavior using a camera (DCC1545M, Thorlabs) and infrared illumination from an LED array (IR045, Clover Electronics). At the end of each imaging session, we removed all the micro-optics from the mouse's head and cleaned the microendoscopes for future reuse.

For large-scale mapping of the cortical retinotopy, we used one arm of the microscope with a low-magnification objective (CFI LU Plan Epi, 0.15 NA  $\times 5$  Nikon). We presented a thin ( $10^\circ$ ) sliding ( $7 \text{ deg} \times \text{s}^{-1}$ ) bar of alternating (temporal frequency, 2 Hz) blue checkerboard (spatial frequency, 0.035 cycles per deg) as described before<sup>13</sup>. The mean luminance of the stimulus at the mouse's eye

was  $\sim 5 \times 10^{10}$  photons  $\times$  mm $^{-2}$   $\times$  s $^{-1}$ , which is  $\sim 3$  orders of magnitude above the threshold sensitivity of the mouse's M-opsin cone and  $\sim 2$  orders of magnitude above the transition threshold from mesopic to photopic vision in mice<sup>28</sup>. We performed two-photon Ca<sup>2+</sup> imaging with a 1-Hz frame acquisition rate over a  $\sim 2.5$ -mm-wide field of view. We imaged for  $\sim 15$  min in awake mice and averaged the responses over all trials. We identified V1 and LM on the basis of their retinotopic maps and the previously published retinotopy of the mouse visual cortex<sup>13</sup>.

For dual-axis two-photon Ca<sup>2+</sup> imaging, we presented a sinusoidal grating on the video monitor for 3 s (0.035 cycles per deg, 1.25 Hz, full screen, 90° orientation steps) interleaved with 3-s gray screen periods. We randomly shuffled orientation angle sequences. We applied spherical altitude correction to sinusoidal gratings to hold spatial frequency and temporal frequency constant throughout the visual field as previously described<sup>13</sup>.

**Statistical and image analyses.** We performed all analyses of data from the dual-axis microscope using custom software written in MATLAB (Mathworks). The first step of analysis computationally unmixes the crosstalk in the photocurrents of the two PMTs. This cross-talk arose because a minority of fluorescence photons emitted at the focus of one imaging arm returned through the collection optics of the other arm. Hence, crosstalk increased when the two focal planes were in nearby brain areas. If one area fluoresced more than the other, the impact of the former channel on the latter was greater than vice versa. In most cases, crosstalk represented  $\sim 5$ – $10\%$  of baseline signals. In all cases, crosstalk was easily unmixed.

For unmixing, we used and empirically validated an independent component analysis (ICA) of the two photocurrent time series. ICA is expressly suited for these purposes and extracts a linear combination of the two channels that represent the two independent sources of fluorescence emission. To empirically validate this approach, we performed control experiments in which we shuttered the laser beam in each optical arm in turn, allowing us to directly measure the crosstalk fluorescence emanating from the other arm. These studies confirmed that the crosstalk magnitude grew linearly with the fluorescence intensity in the opposing arm and could therefore be linearly unmixed. The linear unmixing coefficients determined by ICA were within  $\sim 3$ – $5\%$  of the coefficients measured empirically. This implies the errors in unmixing were  $<0.3\%$  of the baseline fluorescence signals. We thus used the ICA unmixing approach for all imaging studies of neural dynamics.

After unmixing, the next step of analysis accounted for the slight mechanical differences between the forward and backward phases of our double-sided laser line-scanning pattern. These differences arise from the mechanical properties of each pair of scanning mirrors and lead to slight misalignments between the even and odd rows of each image. We found the pixel coordinate transformation that minimized the mismatch between pixels on adjacent lines using least-squares optimization and then fitting a smooth polynomial to the result. To correct for lateral displacements of the brain, we then used affine image registration using a version of the TurboReg algorithm<sup>29</sup> written in C.

To highlight Ca<sup>2+</sup> transients against baseline fluctuations, we used the fact that the two-photon fluorescence increases of GCaMP6 during Ca<sup>2+</sup> transients are many times the s.d. of background noise. Thus, we converted each pixel's fluorescence trace,  $F(t)$ , into a trace of z-scores,  $\Delta F(t)/\sigma$ . Here  $\Delta F(t) = F(t) - F_0$  denotes the pixel's deviation from its mean value,  $F_0$ , and  $\sigma$  denotes the pixel's background noise, which we estimated by taking the minimum of all s.d. values calculated with a sliding 10-s window. After transforming the movie data into this  $\Delta F(t) = F(t) - F_0$  form, we identified neuronal cell bodies and processes using an established cell-sorting algorithm that sequentially applies principal and independent component analyses (PCA and ICA) to extract individual cells' spatial filters and time traces<sup>15</sup>. To obtain a final set of  $\Delta F(t) = F(t) - F_0$  traces, we multiplied each cell's spatial filter with each frame of the raw, motion-corrected fluorescence movie. Using the resulting  $F(t)$  trace we calculated its time-averaged mean,  $F_0$ , and thereby computed  $\Delta F(t)/F_0 = [F(t) - F_0]/F_0$ . To detect individual Ca<sup>2+</sup> transients in the  $\Delta F(t)/F_0$  traces, we applied a fast non-negative

deconvolution<sup>30</sup> to each time trace and identified local maxima in the resulting traces. For cell bodies, we estimated the most likely number of underlying action potentials for each Ca<sup>2+</sup> transient by rounding the value of the deconvolved trace at the local maximum to the nearest integer.

We did not employ statistical methods to predetermine sample sizes. Our sample sizes were similar to those generally employed in the field and sufficient to obtain multiple highly significant results, as reported in the main text. Reported errors are standard errors unless specified otherwise. A **Supplementary Methods Checklist** is available. All assumptions were met for proper usage of both the sign test and Wilcoxon rank-sum test. We used two-sided statistical tests.

The C code of the TurboReg algorithm is available on its author's website<sup>29</sup>. ScanImage<sup>26</sup> is available through the HHMI Janelia Farm Open Wiki. The PCA/ICA algorithm for cell sorting<sup>15</sup> is available on the Mathworks File Exchange. We used FastICA to isolate crosstalk between PMTs. FastICA is also available on its author's website<sup>31</sup>.

**Studies of possible optical crosstalk from out-of-focal plane neurons.** We performed computational and experimental control studies to verify that the axial resolution values (9.8  $\mu$ m and 7.9  $\mu$ m) of our dual-axis microscope sufficed to prevent crosstalk from out-of-focal plane neuronal cell bodies, dendrites and axons.

Computational studies used the measured resolutions and actual three-dimensional anatomic coordinates and Ca<sup>2+</sup> activity traces of layer 2/3 visual cortical neurons, as determined from two-photon imaging data sets acquired in behaving mice (**Supplementary Fig. 3a–c**). These computations predicted that  $>97\%$  of neuronal cell bodies would have 0% crosstalk in the digitized rasters of action potentials detected in the  $\Delta F/F$  traces and that 98.5% of neurons would have  $<5\%$  false-positive spikes due to crosstalk from other cell bodies (**Supplementary Fig. 3d**).

To examine experimentally whether crosstalk from any neural sources (somata, dendrites or axons) might occur, we directly assessed crosstalk levels using a dual laser beam two-photon imaging system to simultaneously record at two different axial resolutions ( $10.4 \pm 0.4 \mu$ m and  $4.0 \pm 0.1 \mu$ m; mean  $\pm$  s.d.,  $n = 3$  beads) the Ca<sup>2+</sup> dynamics of layer 2/3 visual cortical neurons (**Supplementary Fig. 4a**). Comparisons between the two concurrently acquired data sets revealed hardly any discernible differences in the fluorescence ( $\Delta F/F$ ) traces (**Supplementary Fig. 4b**). After applying an event detection algorithm<sup>30</sup> to obtain digitized records, there was no evidence of crosstalk in event traces based on the 10- $\mu$ m-resolution data versus the 4- $\mu$ m-resolution data, as benchmarked by alternating time points in 4- $\mu$ m-resolution traces to estimate the baseline level of statistical uncertainty in the event detection process (**Supplementary Fig. 4c**). Given that the neurons' measured cell-body diameter was  $12.09 \pm 0.05 \mu$ m (mean  $\pm$  s.e.m.;  $n = 339$  layer 2/3 pyramidal cells), it is extremely unlikely that any further improvements in axial resolution to values finer than 4  $\mu$ m would significantly change these conclusions. Please see **Supplementary Figure 4** for further details of these experiments and statistical analyses.

- Madisen, L. *et al.* A robust and high-throughput Cre reporting and characterization system for the whole mouse brain. *Nat. Neurosci.* **13**, 133–140 (2010).
- Hippenmeyer, S. *et al.* A developmental switch in the response of DRG neurons to ETS transcription factor signaling. *PLoS Biol.* **3**, e159 (2005).
- Pologruto, T.A., Sabatini, B.L. & Svoboda, K. ScanImage: flexible software for operating laser scanning microscopes. *Biomed. Eng. Online* **2**, 13 (2003).
- Andermann, M.L., Kerlin, A.M. & Reid, R.C. Chronic cellular imaging of mouse visual cortex during operant behavior and passive viewing. *Front. Cell. Neurosci.* **4**, 3 doi:10.3389/fncel.2010.00003 (2010).
- Naarendorp, F. *et al.* Dark light, rod saturation, and the absolute and incremental sensitivity of mouse cone vision. *J. Neurosci.* **30**, 12495–12507 (2010).
- Thevenaz, P., Ruttimann, U.E. & Unser, M. A pyramid approach to subpixel registration based on intensity. *IEEE Trans. Image Process.* **7**, 27–41 (1998).
- Vogelstein, J.T. *et al.* Fast nonnegative deconvolution for spike train inference from population calcium imaging. *J. Neurophysiol.* **104**, 3691–3704 (2010).
- Hyvärinen, A. Fast and robust fixed-point algorithms for independent component analysis. *IEEE Trans. Neural Netw.* **10**, 626–634 (1999).